metals

MDPI

Article

The Effect of the Rolling Reduction Ratio on the Superelastic Properties of Ti-24Nb-4Zr-8Sn (wt%)

Oliver G. Reed, Benjamin T. Desson, Nicole L. Church * and Nicholas G. Jones

Department of Materials Science and Metallurgy, University of Cambridge, 27 Charles Babbage Road, Cambridge CB3 0FS, UK; or280@cam.ac.uk (O.G.R.); ngj22@cam.ac.uk (N.G.J.)
* Correspondence: nc457@cam.ac.uk

Abstract

Ti-Nb alloys have been under active consideration for superelastic applications in biomedical devices due to their superior biocompatibility compared to NiTi. However, these alloys have been found to be highly sensitive to processing conditions, with many studies measuring different transformation temperatures for the same alloy composition. Several processing factors, including heat treatment times, temperatures and cooling rates, have been investigated. However, the effect of the rolling ratio on superelastic properties has not yet been systematically considered. In this study, samples of Ti-24Nb-4Zr-8Sn (wt%) with varied cold rolling reduction ratios were produced, and the superelastic properties were characterised. After the heat treatment, all samples were found to be predominantly in the metastable cubic β phase, with a small, non-varying volume fraction of the ω phase also present. Electron backscattered diffraction was utilised to measure the resulting texture and grain size in each sample, and these values were correlated to the superelastic properties.

Keywords: rolling; recrystallisation; titanium alloys; phase transformations; electron backscattering diffraction (EBSD); superelasticity

check for updates

Academic Editor: Maciej Motyka

Received: 20 October 2025
Revised: 27 November 2025
Accepted: 28 November 2025
Published: 30 November 2025

Citation: Reed, O.G.; Desson, B.T.; Church, N.L.; Jones, N.G. The Effect of the Rolling Reduction Ratio on the Superelastic Properties of Ti-24Nb-4Zr-8Sn (wt%). *Metals* **2025**, *15*, 1323. https://doi.org/10.3390/met15121323

Copyright: © 2025 by the authors. Licensee MDPI, Basel, Switzerland. This article is an open access article distributed under the terms and conditions of the Creative Commons Attribution (CC BY) license (https://creativecommons.org/licenses/by/4.0/).

1. Introduction

Superelastic alloys have low elastic moduli and can exhibit large recoverable strains, which makes them potential candidate materials for bone replacement implants in the biomedical industry [1–3]. However, the most extensively studied superelastic alloys, based on NiTi, have poor workability at room temperature and can lead to Ni sensitivity in the human body, limiting biocompatibility [1–4]. Ti-Nb-based superelastic alloys have been developed to address these issues, with many showing excellent cold workability and biocompatibility [1–5]. Typically, these alloys comprise a metastable form of the high temperature cubic β phase that can transform to an orthorhombic martensite, α'', on the application of critical stress, σ_{SIM}, or when cooled below the martensite start temperature, M_S [3,6]. On loading, this transformation gives rise to a macroscopic shape change that can dramatically reduce the effective modulus of the alloy. On unloading, the transformation is reversible, with the α'' transforming back to β, recovering the associated deformation. However, the extent of this recovery is poor in some alloys, particularly when loaded to high stresses [2].

To effectively utilise superelastic alloys in commercial applications, the factors affecting σ_{SIM} and the extent of recovery must be known, such that both properties can be tailored to the target application [7,8]. One factor known to influence these properties is composition. Whilst the effect of composition on σ_{SIM} in Ti-Nb alloys has been extensively investigated

for a range of alloying additions [1,2,9–16], compositional changes alone cannot explain the full variation in properties seen in the literature. For example, substantially differing σ_{SIM} values have been reported, even for alloys of the same composition [17].

It has recently been highlighted that the processing route is also an important parameter that influences the transformation behaviour [17–19]. The conventional processing route for Ti-Nb-based alloys involves cold rolling (CR) to a 50–99% reduction ratio, followed by a recrystallisation heat treatment between 700 and 900 °C [6,18–20]. However, variations in cold rolling total reduction ratios (CR ratios) and heat treatment schedules can lead to substantial differences in the microstructural features, such as variations in both the grain size and texture [21,22]. This, in turn, affects the transformation behaviour.

Of these variations in the microstructure, the effect of the grain size is most often reported to affect superelastic properties, with some studies concluding that a larger grain size increases σ_{SIM} [23], whilst others claim it decreases σ_{SIM} [24]. However, the recent literature has highlighted that the route to achieving a variation in grain size may be able to rationalise many of these discrepancies. For example, a negative correlation is observed between grain size and σ_{SIM} only when this reduction in grain size is achieved by increasing the extent of the cold rolling [25]. In contrast, a positive correlation is observed when this variation is achieved via differences in the heat treatment temperature [23]. Instead, when grain sizes are altered by changing the heat treatment time at a constant temperature, minimal variability is seen in σ_{SIM} [20]. This suggests that the reduction ratio and the heat treatment temperature are both critical parameters that affect the transformation behaviour of Ti-Nb-based alloys. Whilst the effect of changing the heat treatment temperature has been investigated [15,23,26], a detailed mechanistic understanding of the effect of changing the CR ratio has yet to be established.

Varying the CR ratio in Ti-Nb alloys has been shown to lead to differences in texture after recrystallisation [21]. Texture strongly influences the superelastic strain that can be achieved on loading, as the transformation strain, ε_t, is very sensitive to the crystallographic direction. For example, in the Ti-Nb system the transformation strain has been experimentally shown to be largest when a grain is loaded along the $<101>_\beta$ directions [3,6,11]. This observation is supported by theoretical calculations that determined the shape change during transformation [27]. However, the influence of texture on other aspects of the transformation, such as σ_{SIM}, is less well studied.

Despite this, insights into the effect of texture on σ_{SIM} can be inferred from thermodynamic principles. During loading, the work performed, G, by the transformation can be given by Equation (1) [28]:

$$G = \sigma_{SIM} \times \varepsilon_t \quad (1)$$

The principle of maximum work states that the variant that forms at the lowest stress, σ_{SIM}, will be that with the largest ε_t along the loading direction, in order to generate the required driving force [28]. Therefore, σ_{SIM} is expected to vary inversely with ε_t [28]. Such a relationship has been observed experimentally in one study on NiTi [29], where samples were generated with different textures along the loading direction by extracting them from the same rolled sheet at different orientations. Samples that had smaller transformation strains showed larger σ_{SIM} [29], in agreement with the principle of maximum work. However, in other studies on NiTi, contrasting results were obtained with both the largest transformation strain and greatest σ_{SIM} measured when the tensile axis was along the $<101>_{B2}$ directions [30,31].

A relationship between texture and σ_{SIM} has also been observed in Ti-based metastable β superelastic alloys. For example, a study on a Ti-Zr-Nb-Sn alloy showed σ_{SIM} decreasing with the CR ratio, with the development of a strong $\{001\}_\beta <101>_\beta$-type texture highlighted as a possible cause of the change [32]. In this study, the transformation strain increased as

σ_{SIM} fell, consistent with the principle of maximum work [28]. Despite the study suggesting an inverse relationship between the CR ratio and σ_{SIM}, positive correlations have also been reported. One study on the effect of the grain size on σ_{SIM} demonstrated an increase in σ_{SIM} with a greater CR reduction ratio [25]. The transformation strain also increased, suggesting that there may have also been an associated change in texture, although this was not measured. Furthermore, the increase in σ_{SIM} with ε_t does not conform to the principle of maximum work. This is not necessarily surprising as the principle of maximum work was formulated for analysing single variants in a single grain, and the situation is more complex when multiple variants are forming in several grains of different orientations [28,33]. Therefore, thermodynamic principles cannot fully explain the effect of the CR ratio and texture on σ_{SIM}.

To utilise the full potential of these alloys, the relationship between the CR ratio and σ_{SIM} needs to be established. However, there have been few systematic studies of the effect of different cold rolling ratios on superelastic properties of Ti-Nb-based alloys, with many studies failing to report the CR ratio used or measure the crystallographic texture. To address this issue, here, strips of a commercial Ti-Nb-based alloy, Ti2448 (actual composition of Ti-23.82Nb-3.85Zr-7.52Sn (wt%) [20]), were cold rolled to reductions between 50 and 90% followed by an identical recrystallisation heat treatment. The superelastic properties were obtained and related to the texture and grain size in order to determine the mechanism driving changes in such properties.

2. Methods

Sections of a commercially produced bar of Ti2448 were cut using electro discharge machining (EDM) into cuboidal bars with initial dimensions of 20 mm (length, along RD) × 10 mm (transverse direction, TD) × initial thickness (ND). The initial thickness was varied to achieve the target total rolling reduction ratio (CR ratio), as shown in Table 1, with each bar cold rolled to a final thickness of 0.7 mm. The reduction was achieved through multiple passes with a reduction of ~10% per pass. The number of passes ranged from 7 (CR50) to 20 (CR90). As the rolling process was performed at ambient temperature, no recovery or recrystallisation was expected between rolling passes, and, as such, the total reduction ratio serves as a meaningful comparative parameter, independent of the number of passes or the absolute reduction achieved in each pass. The rolling process utilised a Dima Maschinen Type K 65 E (Dima Maschinen, Esslingen am Neckar, Germany) rolling mill with a roll diameter of 64 mm and a rotational speed of 30 RPM. The workpiece temperature was monitored using a Flir TG268 thermal imaging camera (Flir, Wilsonville, Oregon, USA), and the peak temperature reached did not exceed 50 °C.

Table 1. Table showing initial bar thickness and cold rolling reduction ration (CR ratio) for each condition.

Sample	Initial Thickness/mm	Final Thickness/mm	CR Ratio/%
CR50	1.4	0.7	50
CR60	1.8	0.7	60
CR70	2.3	0.7	70
CR80	3.5	0.7	80
CR90	7	0.7	90

EDM was used to cut tensile samples with a gauge cross-section of (1.4 × 0.5) mm^2 from the rolled strips, with the tensile axis aligned parallel to the rolling direction (RD), along with (5 × 5) mm^2 square samples for microstructural characterisation. All samples

were ground to a 15 µm finish to remove the re-cast layer from EDM, cleaned using ethanol, wrapped in Ta foil and sealed in an evacuated quartz tube. The samples were then heat treated together for 5 min at 900 °C, followed by quenching in ice water, with the samples remaining inside the intact quartz tube. Microstructural and mechanical characterisation was performed on the samples in this recrystallised condition.

To identify the constituent phases present, synchrotron X-ray diffraction (SXRD) patterns were obtained on the I12 beamline at Diamond Light Source (Harwell, UK) in a transmission Debye Scherrer geometry. The beam energy was ascertained using a NIST CeO_2 powder (Cerac Inc. (Milwaukee, WI, USA)) standard at different distances, and the incident monochromatic beam had a wavelength of 0.15678 Å [34–36]. Diffraction patterns were collected using a Pilatus 2M detector (Dectris AG, Baden-Datwill, Switzerland), with an exposure time of 2 s. The 2D diffraction data were reduced to 1D by azimuthal integration over the full angular range using DAWN v2.37 software [37,38].

Characterisation of the texture and grain size was achieved through EBSD. Samples were mounted such that the observed surface was the RD-TD plane (the plane normal to the normal direction, ND). Samples were polished using a 0.04 µm colloidal silica suspension, buffered to pH 7 by H_2O_2. EBSD measurements were obtained using an Oxford Instruments Symmetry detector on a Zeiss GeminiSEM 300 (Carl Zeiss AG, Oberkochen, Germany). Measurements were conducted using a 120 µm aperture, an accelerating voltage of 25 kV, a step size of 2 µm and a dwell time of 4 ms. Grain area distributions, inverse pole figure-z (IPFz) maps and IPF triangles were all generated using AZtecCrystal software v3.3. The IPF triangles were plotted relative to the rolling (RD), normal (ND) and transverse (TD) directions of the cold rolling operation, with the ND aligned with the z direction of the sample during acquisition. The grain areas were used to generate equivalent circular area diameters. These values were plotted as histogram distributions where the *y*-axis is the probability density (normalised by the total grain count and bin width). The distributions were fitted with log-normal functions, in which the mean value and the standard error in the mean were calculated, following the methodology in [39].

The mechanical and superelastic properties of each condition were assessed using incremental load tests on an Instron 3367B test frame (Instron, Norwood, MA, USA) with a 12.5 mm contact extensometer and a 30 kN load cell. Samples with the tensile axis aligned along RD were pre-loaded to 25 MPa and then cyclically loaded at a rate of 4 MPa s^{-1} to a peak stress that increased by 25 MPa each cycle. The envelope of the cyclic stress–strain data was used as a proxy for the tensile behaviour, consistent with the approach outlined in [40,41]. The envelope stress–strain data were used to determine the onset of transformation, σ_{SIM}, and the onset of plastic deformation by slip, σ_y. The former was determined as the stress at which the curve deviated from the linear section by 0.05% strain, and the latter was the deviation from the linear section corresponding to elastic loading of the martensite by 0.2% strain. The reported uncertainty for stress values, including σ_y and σ_{SIM}, is primarily determined by the error in measuring the cross-sectional area of the tensile samples. Based on the dimensional measurements, the uncertainty in the stress values was calculated to be ±5%. σ_{rec} is defined as the loading stress for the last cycle, which was fully recoverable on unloading, and ε_{rec} is the recovered strain in this cycle, consistent with approaches to measuring recoverability in the literature [40,42,43].

One tensile sample was tested for each cold rolling ratio condition (CR50 to CR90). A subsequent replicate test on the CR80 condition confirmed that the mechanical response and the determined σ_{SIM} and σ_y values were consistent with the initial measurement, validating the repeatability of the results presented.

3. Results and Discussion

To determine the phase constitution of the alloy in each condition, SXRD patterns were obtained, as displayed in Figure 1. The alloy was found to be predominately single-phase in all conditions at room temperature, with peaks consistent with the β phase [6,20,21]. The intensities of the β peaks do not match an ideal powder sample prediction, which indicates that a crystallographic texture is present within the sample, as would be expected from cold rolling and recrystallisation [21]. A weak broad peak was observed at 6.4° 2θ in all patterns, indicative of a small volume fraction of the ω phase [17]. The peak is of a similar intensity in the pattern for each condition. Ti-2448 is known to be less susceptible to the formation of ω, and the reported trends within this study are not expected to be driven by variation in the ω volume fraction or morphology.

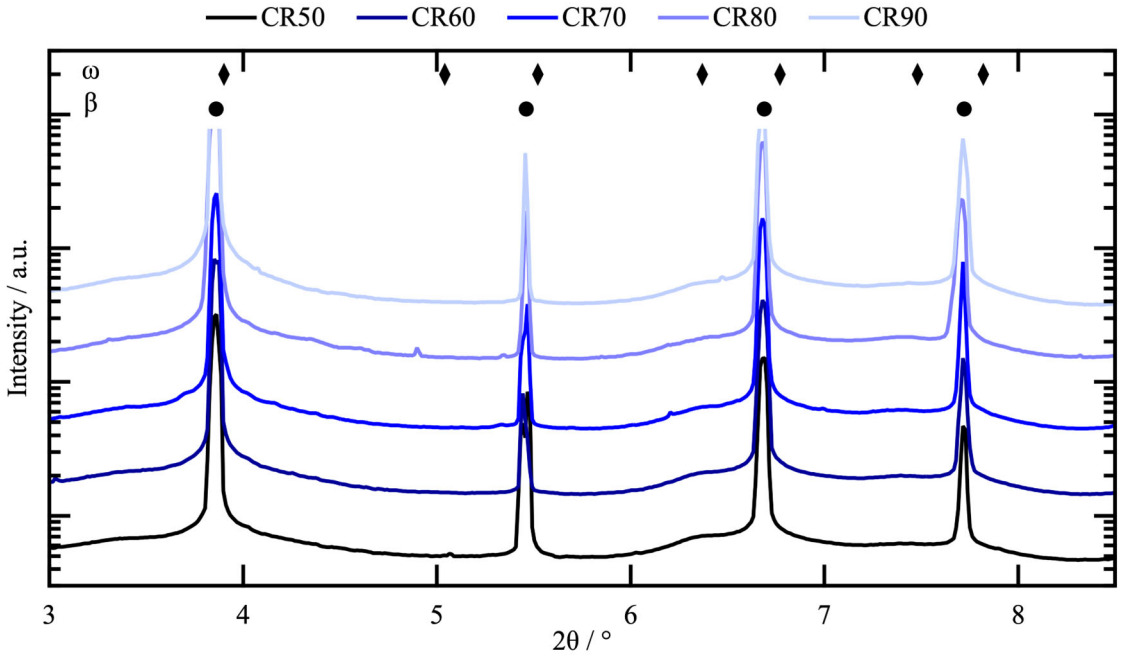


Figure 1. SXRD patterns of each alloy in the recrystallised condition, with the cold rolling reduction ratio before recrystallisation as indicated for each sample. The positions of reflections for the β and ω phases are indicated by the symbols at the top of the figure. Note that for the CR80 sample, some signal from the sample holder was detected (Al). These peaks were removed from the baseline.

To fully characterise this texture, as well as obtain the grain size, EBSD data were collected from each condition. The IPF maps are shown in Figure 2, with the orientation of each grain relative to the ND indicated by its colour on the IPF triangle. All conditions showed equiaxed grains of a single phase, consistent with the results of the SXRD. The texture can be analysed by considering the IPF triangles, displayed in Figure 3. The texture observed is with the $<101>_{\beta}$ directions aligned along the RD and the $<111>_{\beta}$ directions aligned with the ND. This texture of $\{111\}_{\beta}<101>_{\beta}$ is reported in many bcc alloy systems after cold rolling and recrystallisation, including in previous studies of Ti-Nb alloys and Ti2448 [21,22,43,44]. There was a larger proportion of grains showing a close alignment of a $<101>_{\beta}$ direction with the RD when rolled to larger total reduction ratios (CR ratios), indicating a stronger recrystallisation texture.

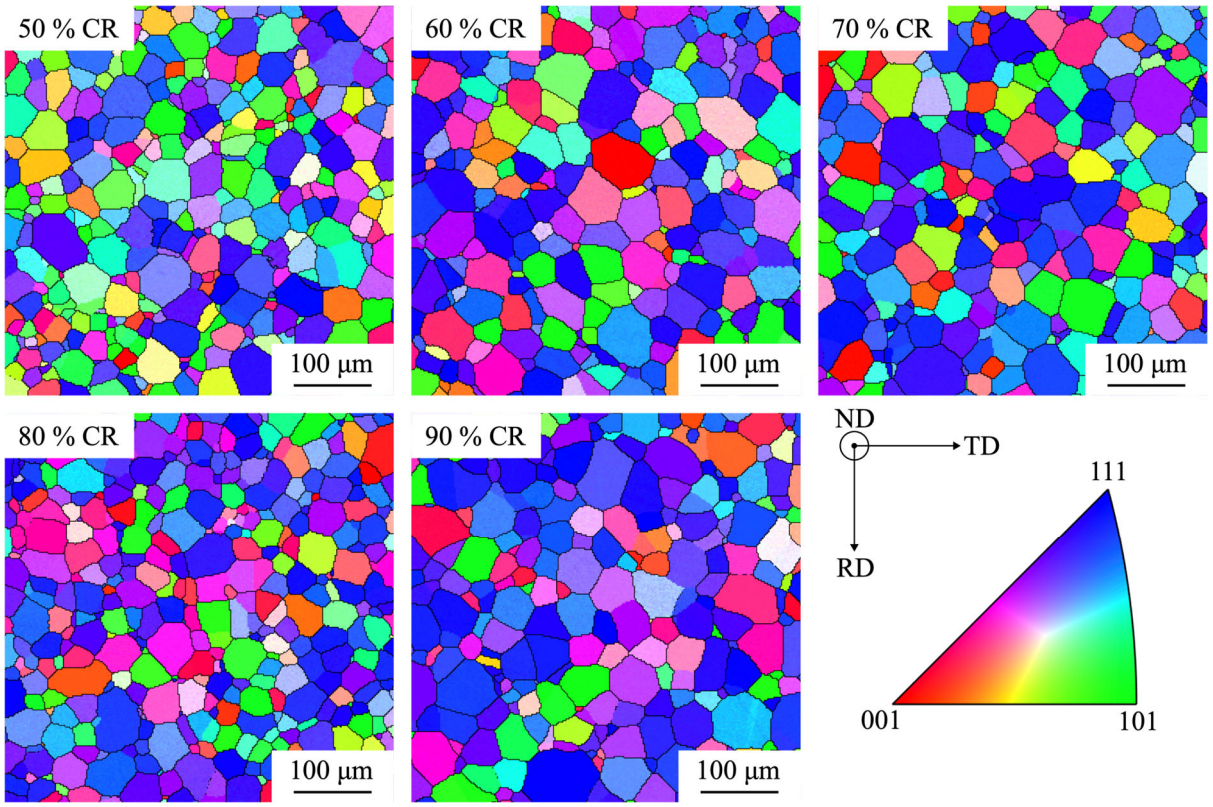


Figure 2. IPF maps of each condition, with the colour of each grain giving its corresponding orientation in the ND, using the colour triangle shown.

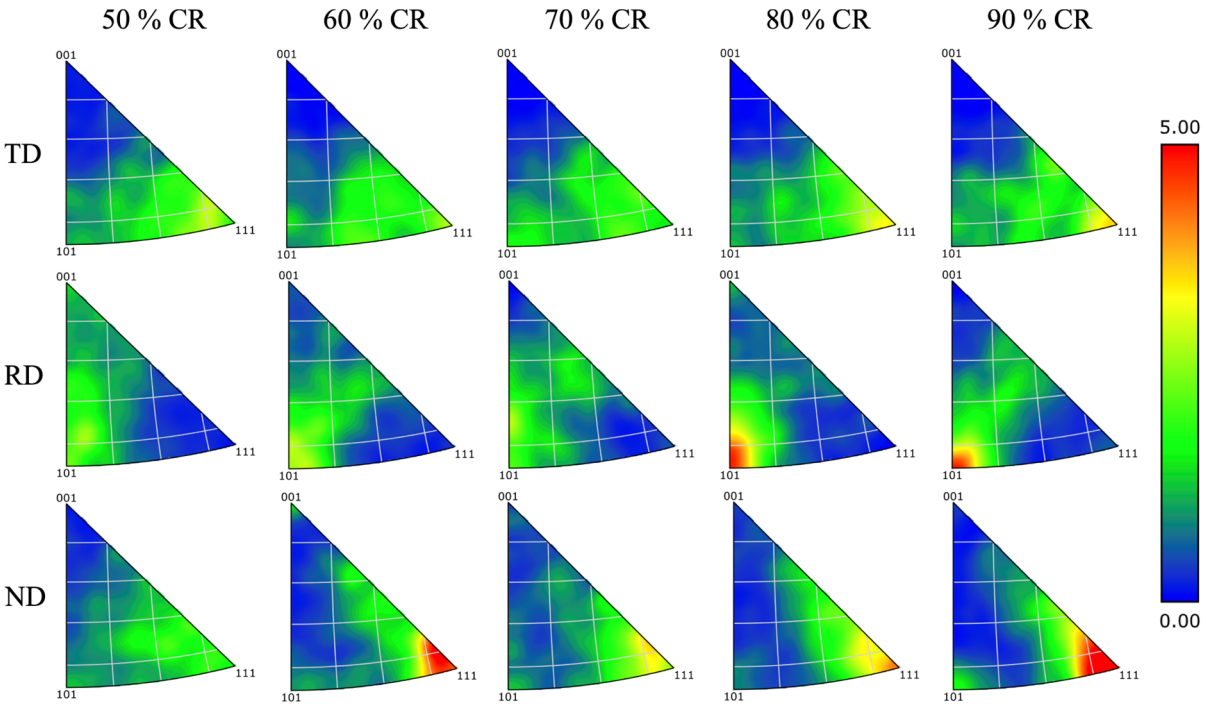


Figure 3. IPF triangles showing the recrystallisation texture of each condition in the transverse direction (TD), rolling direction (RD) and normal direction (ND).

To assess if the grain size could be affecting the superelastic properties, equivalent circular area diameters were obtained for each grain, and these values were plotted as histograms for each condition. These distributions are shown in Figure 4 and were used to

quantify the average grain size, shown alongside as a function of the CR ratio (Figure 4f). It can be seen that there is no significant or systematic variation in the average grain size with the CR ratio, contrary to the results of previous work [21]. Furthermore, the shape and spread of the histograms are statistically similar across all conditions, indicating that the overall grain size distribution is not significantly influenced by the CR ratio in this study. This can be seen as all distributions have similar standard errors in the mean.

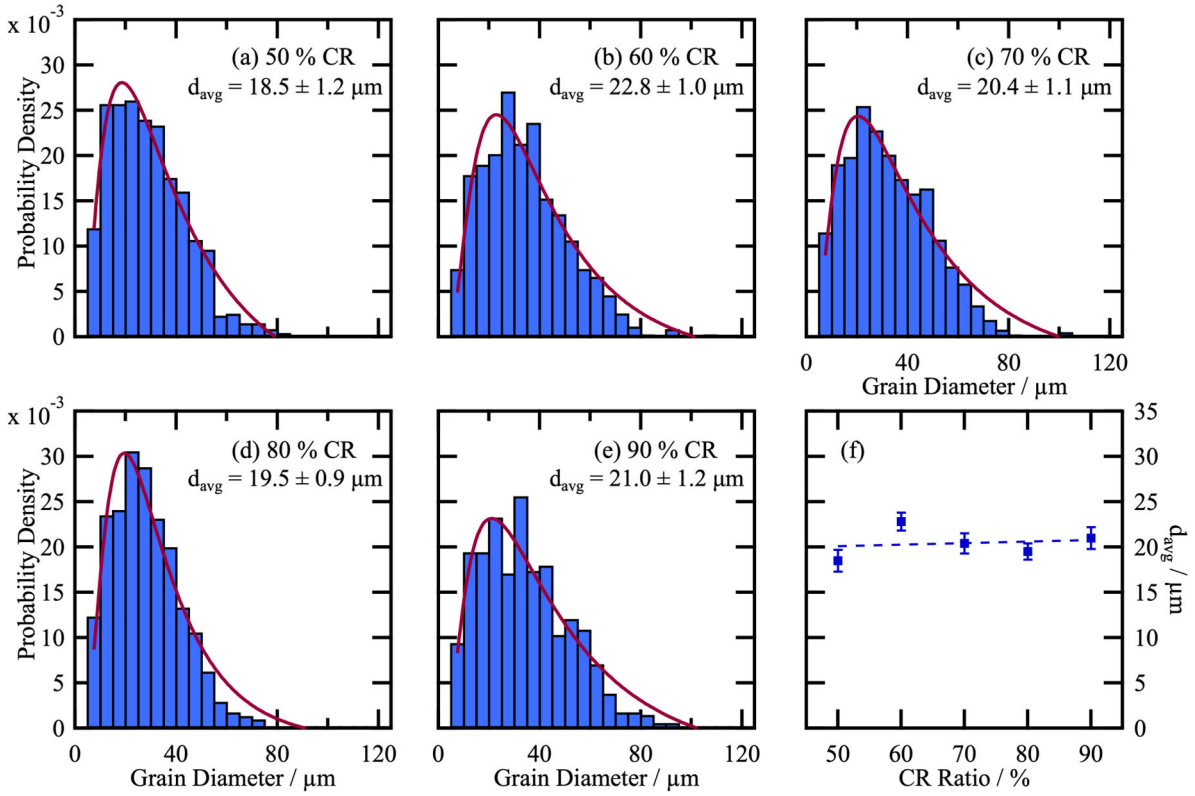


Figure 4. (**a**–**e**) Equivalent circular area diameter normalised histograms for each condition and (**f**) average equivalent circular area diameter against CR ratio, with a dotted line indicating the line of best fit.

To determine the superelastic and mechanical properties, an incremental load test was performed for the material in each condition. This type of test is routinely used, within the literature of Ti-Nb alloys, to probe the superelastic behaviour and extent of recovery across a range of stresses. The tensile response is plotted for each condition in Figure 5. During loading, all conditions initially show a linear elastic loading regime, followed by a decrease in gradients consistent with the martensitic transformation from β to α'' [3,6]. This transformation results in a region of a lower gradient, which is the superelastic plateau. Beyond this plateau, there is an increase in the gradient and a second linear region, which is reported to correspond to the elastic loading of the newly formed α'' martensite. Finally, a decrease in the gradient occurs beyond σ_y, consistent with plastic deformation occurring due to dislocation motion (slip) [3,7,27]. The onset of the martensitic transformation, σ_{SIM}, and σ_y were determined from the envelope plot (Figure 5), and their values are summarised in Table 2, with the variation with the CR ratio shown in Figure 6.

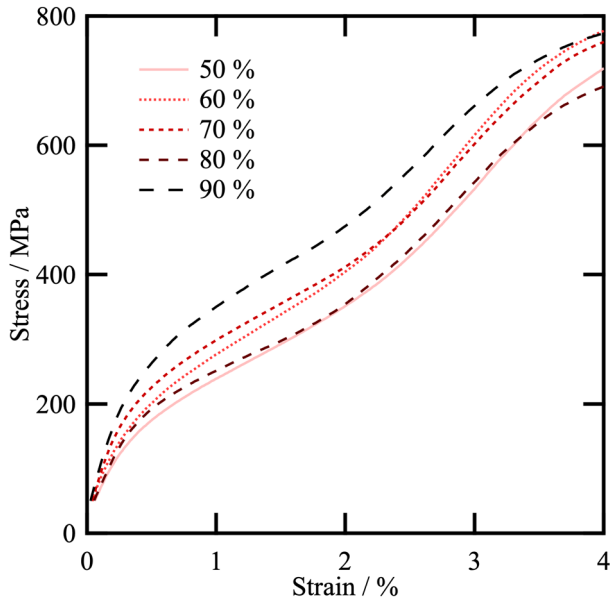


Figure 5. The envelopes of the incremental load tests for each condition.

Table 2. The yield stress, σ_y, and the stress at the onset of transformation, σ_{SIM}, for each condition. The error in each value is ±5%.

Sample	σ_y/MPa	σ_{SIM}/MPa
CR50	726	137
CR60	760	145
CR70	748	171
CR80	716	164
CR90	747	192

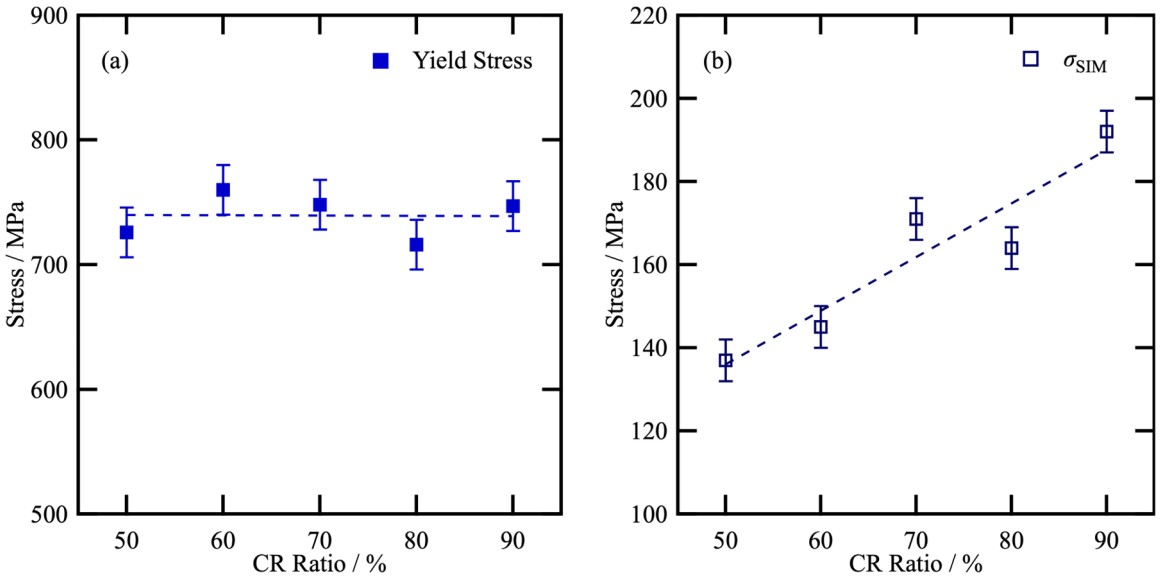


Figure 6. (**a**) Variation in yield stress with CR ratio, indicating no correlation in this study; (**b**) variation in σ_{SIM} with CR ratio, indicating there is a positive correlation. Error bars in both panels represent ±5%, derived from the uncertainty in the sample cross-sectional area measurement.

It was found that the yield stress (σ_y, Figure 6a) showed minor variations across the series. However, when considering the ±5% measurement uncertainty, no systematic trend or statistically significant difference was observed, indicating that the CR ratio does not

influence the onset of plastic slip in this range. This is as expected, as the grain size and composition are unchanged across the series, and any changes in dislocation density are likely to have a negligible effect due to the slow rate of work hardening in β Ti alloys [3,45]. However, there was a positive correlation between the CR ratio and σ_{SIM} (Figure 6b), indicating that the CR ratio did affect the superelastic properties of the material. While this trend is clear and systematic, there is a minor deviation where the σ_{SIM} for the CR80 sample is slightly lower than that for the CR70 sample. This minor fluctuation is further explored in the discussion of competing mechanisms below.

The positive correlation of σ_{SIM} with the CR ratio cannot be driven by compositional changes as all samples are from the same commercially supplied material and have been heat treated identically. Some literature has suggested that changes in grain size with the CR ratio may affect σ_{SIM} [25], although this is disputed [20], with the most recent study suggesting that the method of grain refining may be driving changes in σ_{SIM} rather than the grain size itself. In the present study, there was no variation in the grain size across the series; hence, it cannot be responsible for the observed trends.

Here, a larger CR ratio led to a stronger recrystallisation texture, which is in agreement with the current theories of recrystallisation and previous work on Ti2448 [21,22,32,46]. Specifically, there was a stronger alignment of the $<101>_{\beta}$ directions along the RD, which was the tensile direction of the mechanically tested samples. As the changes in σ_{SIM} in this study cannot be due to changes in the composition or grain size, the most likely cause of the changes in σ_{SIM} is textural differences between the different conditions. This study showed that in Ti2448, a stronger alignment of $<101>_{\beta}$ with the tensile axis increased the σ_{SIM}. Since $<101>_{\beta}$ was also the direction of the maximum transformation strain [3,11], this trend is inconsistent with the principle of maximum work. Other studies on Ti-Nb alloys also found an increase in both the transformation strain and σ_{SIM} as the CR ratio increased [25,28]. This highlights that, in polycrystalline Ti–Nb alloys, σ_{SIM} is not governed solely by the transformation strain magnitude and the principle of maximum work [42].

To identify the mechanism behind this increase in σ_{SIM}, the individual cycles of the incremental load test were analysed, as shown in Figure 7. It was observed that for the lower CR ratio samples, in the first cycles loading above σ_{SIM}, no recovery was observed. A superelastic recovery from α'' to β is only seen in later cycles. This indicates that the α'' is being stabilised in some regions of the material more than others, which has previously been linked to inhomogeneity in the sample [42]. In these regions, the more stabilised α'' can form at lower macroscopically applied stresses, resulting in a lower measured σ_{SIM}. This α'' remains in the material on unloading, leading to incomplete recovery and plastic strain accumulation. There is no compositional inhomogeneity expected in the heat-treated sample [44], and, instead, internal stress inhomogeneity may be driving the variation in stability [42]. Inhomogeneity in the internal stress state can develop during cold rolling and subsequent recrystallisation [18]. As lower CR ratios result in lower dislocation densities on rolling than higher ratios, this can lead to a reduced driving force for recrystallisation. As such, lower CR ratios may result in incomplete recovery and a higher degree of stress inhomogeneity after recrystallisation [46]. Recent studies have shown that such stress heterogeneity plays a key role in stabilising α'' and lowering σ_{SIM}, even when the crystallographic texture is favourable [47,48]. In addition, stress inhomogeneity during loading can also arise from texture variations between neighbouring grains, with more random textures producing greater local stress mismatches, lowering σ_{SIM} in these regions [17,49]. This is also expected to be exacerbated in lower CR ratio samples, which show greater texture variations in recrystallised samples. Despite these trends, further research is required to determine whether the local stress inhomogeneity is predominately produced during recrystallisation or from textural differences during loading.

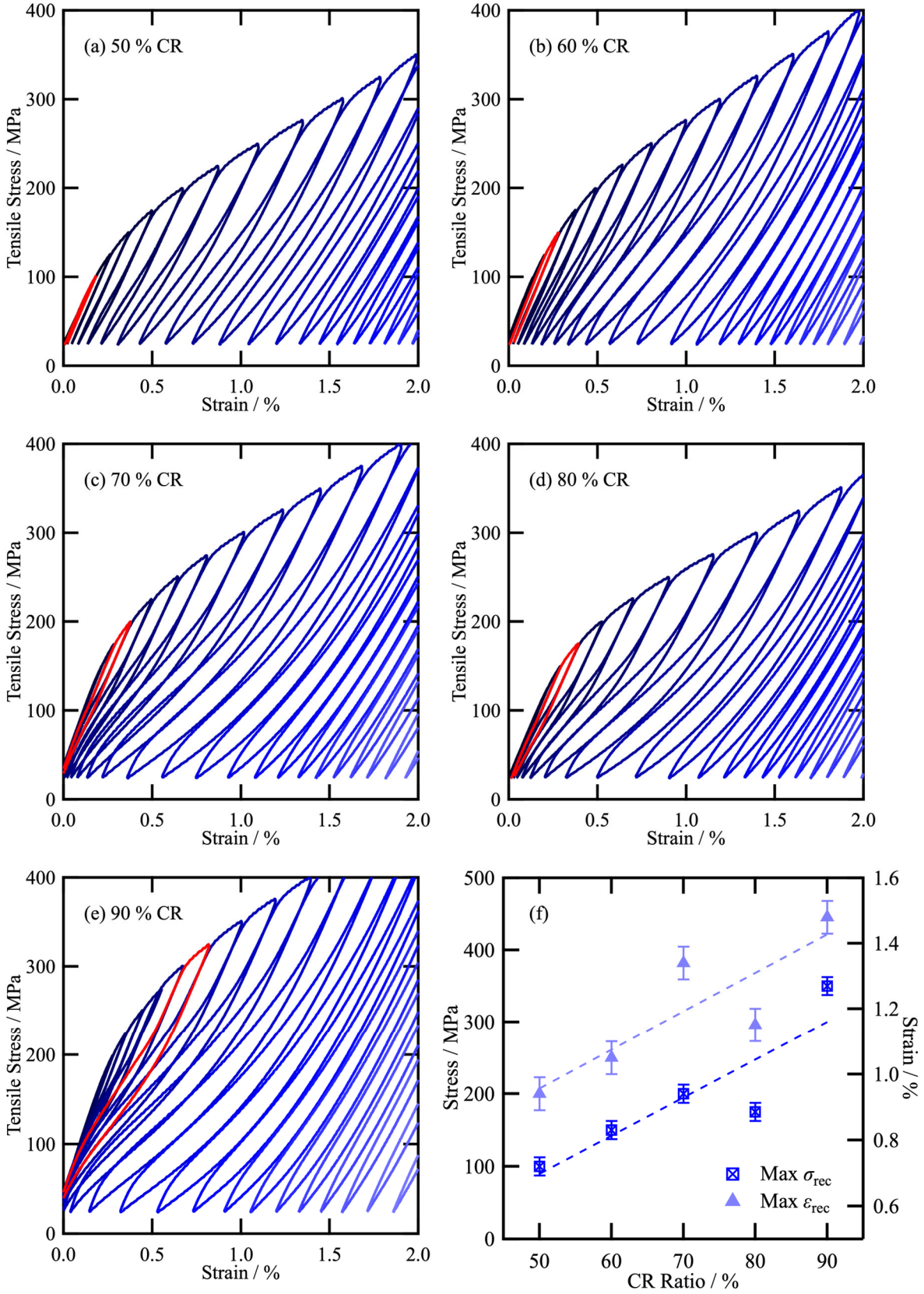


Figure 7. (**a**–**e**) Individual cycles of the incremental load test for each condition. The cycle with the highest stress that still shows full recovery is highlighted in red for each condition. (**f**) The stress and strain reached during this cycle against the CR ratio.

The minor deviation observed in the CR80 condition, where σ_{SIM} falls below the CR70 value, serves as a possible example of this competition. While a larger CR ratio generally

leads to a more favourable texture for transformation strain and higher σ_{SIM}, the CR80 sample may have locally retained a slightly larger degree of internal stress inhomogeneity during recrystallisation. Internal stress inhomogeneity is known to create localised regions where the α'' martensite phase is more easily stabilised, allowing the phase to form at a lower macroscopic applied stress. Therefore, this local heterogeneity could be responsible for the observed dip in σ_{SIM} for the CR80 condition, effectively overriding the effect of the stronger overall texture. This finding reinforces the conclusion that internal stress plays a critical role in the macroscopic measurement of σ_{SIM}.

To determine the recoverability of the different conditions, the individual load–unload cycles may be considered [40,42,43]. The last cycle at which the martensite is still fully recoverable is shown in red for each condition in Figure 7. The stress (σ_{rec}) and corresponding peak recoverable strain (ϵ_{rec}) reached in these cycles was extracted (Figure 7f), and both show a positive correlation with the CR ratio. There is a minor local deviation observed for the CR80 sample, where σ_{rec} and ϵ_{rec} drop below the CR70 values, which exactly mirrors the similar local drop observed for σ_{SIM} in Figure 6b.

The positive correlation between the recovery strain and CR ratio is likely to be the result of the stronger $<101>_{\beta}$ texture exhibited by samples cold rolled to a larger reduction ratio. In the literature, an alignment of $<101>_{\beta}$ along the tensile direction is widely reported to result in the largest transformation strains and largest recoverable strains [3,6,11].

The positive correlation between the maximum recovery stress and the CR ratio can be related to the variation in σ_{SIM} [50]. It is known that during transformation, from β to α'', there is dislocation generation to maintain geometric continuity at the phase boundaries [51,52]. It has been reported that these dislocations act to increase the internal stress, stabilising the martensitic phase [42]. A larger applied stress above σ_{SIM} leads to a greater transformation of β to α'', more interfaces and a greater internal stress build up. At a critical value, the internal stress accumulated due to transformation will be large enough to stabilise a small volume fraction of α'' when the sample has been macroscopically unloaded [42]. If an alloy has a higher onset stress for transformation, larger stresses will be required to generate the internal stress required to stabilise the α'' such that it is retained on unloading [50]. As such, as positive correlation between σ_{SIM} and σ_{rec} is expected, as was observed in this study. The consistency of the CR80 data point across both figures (lower σ_{SIM} and lower σ_{rec}) supports the proposed mechanism that variations in σ_{SIM} directly control the stress required to destabilise the martensite and cause retained strain. Overall, these findings underscore the complex interplay between the texture, internal stress distribution and transformation behaviour in Ti2448, highlighting the importance of the processing history in tailoring superelastic performance. The observed consistency across all key superelastic metrics, even for the minor fluctuation at CR80, confirms that the underlying microstructural factors (of the texture and stress state) drive these properties collectively.

4. Conclusions

This study provides a systematic investigation of the positive correlation between cold rolling reduction ratios before recrystallisation and the stress required for the onset of transformation in Ti2448. This is because a larger reduction ratio results in a stronger texture, in particular, a stronger alignment of a $<101>_{\beta}$ direction along the rolling direction and hence the tensile axis. This study demonstrates that in Ti2448, a stronger $<101>_{\beta}$ recrystallisation texture both raises σ_{SIM} and enhances the transformation strain. The simultaneous increase in the transformation strain and σ_{SIM} contradicts the principle of maximum work, which assumes single-variant transformation behaviour, and indicates the need to consider the full polycrystalline texture, as well as the internal stress state when

evaluating σ_{SIM}. This understanding allows for further refined control of the transformation in these alloys, which is crucial to their commercial uptake.

Author Contributions: O.G.R.: Conceptualization, Methodology, Formal Analysis, Investigation, Validation, Writing—Original Draft, Visualisation. B.T.D.: Methodology, Formal Analysis, Investigation. N.L.C.: Conceptualization, Methodology, Validation, Writing—Original Draft, Supervision. N.G.J.: Conceptualization, Methodology, Formal Analysis, Investigation, Validation, Resources, Writing—Review and Editing, Supervision, Project Administration, Funding Acquisition. All authors have read and agreed to the published version of the manuscript.

Funding: This research received no external funding.

Data Availability Statement: The underlying research data required to reproduce these findings are available from the University of Cambridge repository (DOI: 10.17863/CAM.122424).

Acknowledgments: Diamond Light Source is acknowledged for its provision of the beamtime under MG40294.

Conflicts of Interest: The authors declare no conflict of interest.

References

1. Al-Zain, Y.; Kim, H.Y.; Hosoda, H.; Nam, T.H.; Miyazaki, S. Shape memory properties of Ti-Nb-Mo biomedical alloys. *Acta Mater.* **2010**, *58*, 4212–4223. [CrossRef]
2. Kim, H.; Miyazaki, S. Several Issues in the Development of Ti–Nb-Based Shape Memory Alloys. *Shape Mem. Superelast.* **2016**, *2*, 380–390. [CrossRef]
3. Kim, H.Y.; Miyazaki, S. Martensitic Transformation and Superelastic Properties of Ti-Nb Base Alloys. *Mater. Trans.* **2015**, *56*, 625–634. [CrossRef]
4. Ijaz, M.F.; Kim, H.Y.; Hosoda, H.; Miyazaki, S. Superelastic properties of biomedical (Ti-Zr)-Mo-Sn alloys. *Mat. Sci. Eng. C-Mater.* **2015**, *48*, 11–20. [CrossRef]
5. Ma, J.; Karaman, I.; Maier, H.J.; Chumlyakov, Y.I. Superelastic cycling and room temperature recovery of Ti74Nb26 shape memory alloy. *Acta Mater.* **2010**, *58*, 2216–2224. [CrossRef]
6. Kim, H.Y.; Ikehara, Y.; Kim, J.I.; Hosoda, H.; Miyazaki, S. Martensitic transformation, shape memory effect and superelasticity of Ti-Nb binary alloys. *Acta Mater.* **2006**, *54*, 2419–2429. [CrossRef]
7. Duerig, T.W.; Melton, K.N.; Stöckel, D.; Wayman, C.M. *Engineering Aspects of Shape Memory Alloys*; Taylor & Francis: Oxfordshire, UK, 1990.
8. Jani, J.M.; Leary, M.; Subic, A.; Gibson, M.A. A review of shape memory alloy research, applications and opportunities. *Mater. Design* **2014**, *56*, 1078–1113. [CrossRef]
9. Hao, Y.L.; Li, S.J.; Sun, S.Y.; Yang, R. Effect of Zr and Sn on Young's modulus and superelasticity of Ti-Nb-based alloys. *Mat. Sci. Eng. A* **2006**, *441*, 112–118. [CrossRef]
10. Ijaz, M.F.; Kim, H.Y.; Hosoda, H.; Miyazaki, S. Effect of Sn addition on stress hysteresis and superelastic properties of a Ti-15Nb-3Mo alloy. *Scr. Mater.* **2014**, *72*, 29–32. [CrossRef]
11. Kim, H.; Tobe, H.; Kim, J.; Miyazaki, S. Crystal Structure, Transformation Strain, and Superelastic Property of Ti–Nb–Zr and Ti–Nb–Ta Alloys. *Shape Mem. Superelast.* **2015**, *1*, 107–116. [CrossRef]
12. Kim, H.Y.; Hashimoto, S.; Kim, J.I.; Inamura, T.; Hosoda, H.; Miyazaki, S. Effect of Ta addition on shape memory behavior of Ti-22Nb alloy. *Mat. Sci. Eng. A* **2006**, *417*, 120–128. [CrossRef]
13. Kim, J.I.; Kim, H.Y.; Inamura, T.; Hosoda, H.; Miyazaki, S. Shape memory characteristics of Ti-22Nb-(2-8)Zr(at.%) biomedical alloys. *Mat. Sci. Eng. A* **2005**, *403*, 334–339. [CrossRef]
14. Matsumoto, H.; Watanabe, S.; Hanada, S. Beta TiNbSn alloys with low young's modulus and high strength. *Mater. Trans.* **2005**, *46*, 1070–1078. [CrossRef]
15. Pavon, L.L.; Kim, H.Y.; Hosoda, H.; Miyazaki, S. Effect of Nb content and heat treatment temperature on superelastic properties of Ti-24Zr-(8-12)Nb-2Sn alloys. *Scr. Mater.* **2015**, *95*, 46–49. [CrossRef]
16. Wei, L.S.; Kim, H.Y.; Koyano, T.; Miyazaki, S. Effects of oxygen concentration and temperature on deformation behavior of Ti-Nb-Zr-Ta-O alloys. *Scr. Mater.* **2016**, *123*, 55–58. [CrossRef]
17. Church, N.L.; Talbot, C.E.P.; Fairclough, S.M.; Jones, N.G. The total stress approach to martensitic transformations in Ti–Nb-based alloys. *Commun. Mater.* **2025**, *6*, 254. [CrossRef]

18. Church, N.L.; Talbot, C.E.P.; Jones, N.G. On the Influence of Thermal History on the Martensitic Transformation in Ti-24Nb-4Zr-8Sn (wt%). *Shape Mem. Superelast.* **2021**, *7*, 166–178. [CrossRef]
19. Kim, H.Y.; Kim, J.I.; Inamura, T.; Hosoda, H.; Miyazaki, S. Effect of thermo-mechanical treatment on mechanical properties and shape memory behavior of Ti-(26-28) at.% Nb alloys. *Mat. Sci. Eng. A* **2006**, *438*, 839–843. [CrossRef]
20. Church, N.L.; Hildyard, E.M.; Jones, N.G. The influence of grain size on the onset of the superelastic transformation in Ti-24Nb-4Sn-8Zr (wt%). *Mat. Sci. Eng. A* **2021**, *828*, 142072. [CrossRef]
21. Yang, Y.; Castany, P.; Cornen, M.; Thibon, I.; Prima, F.; Gloriant, T. Texture investigation of the superelastic Ti-24Nb-4Zr-8Sn alloy. *J. Alloy. Compd.* **2014**, *591*, 85–90. [CrossRef]
22. Humphreys, F.J. *Recrystallization and Related Annealing Phenomena*; Elsevier: Kidlington, UK, 2004.
23. Tan, Y.B.; Liu, W.C.; Xiang, S.; Zhao, F.; Liang, Y.L. Effect of Grain Size on Stress-Induced Martensitic Transformation in Solution-Treated 51.1Zr-40.2Ti-4.5Al-4.2V Alloy. *Met. Mater. Trans. A.* **2018**, *49*, 6040–6045. [CrossRef]
24. Jiang, X.J.; Zhao, H.T.; Han, R.H.; Zhang, X.Y.; Ma, M.Z.; Liu, R.P. Grain refinement and tensile properties of a metastable TiZrAl alloy fabricated by stress-induced martensite and its reverse transformation. *Mat. Sci. Eng. A* **2018**, *722*, 8–13. [CrossRef]
25. Zhang, D.C.; Lin, J.G.; Wen, C. Influences of recovery and recrystallization on the superelastic behavior of a β titanium alloy made by suction casting. *J. Mater. Chem. B* **2014**, *2*, 5972–5981. [CrossRef] [PubMed]
26. Takahashi, E.; Sakurai, T.; Watanabe, S.; Masahashi, N.; Hanada, S. Effect of heat treatment and sn content on superelasticity in biocompatible TiNbSn alloys. *Mater. Trans.* **2002**, *43*, 2978–2983. [CrossRef]
27. Otsuka, K.; Wayman, C.M. *Shape Memory Materials*, 1st ed.; Cambridge University Press: Cambridge, UK, 1998.
28. Patel, J.R.; Cohen, M. Criterion for the action of applied stress in the martensitic transformation. *Acta Met. Mater.* **1953**, *1*, 531–538. [CrossRef]
29. Grassi, E.N.D.; Chagnon, G.; de Oliveira, H.M.R.; Favier, D. Anisotropy and Clausius-Clapeyron relation for forward and reverse stress-induced martensitic transformations in polycrystalline NiTi thin walled tubes. *Mech. Mater.* **2020**, *146*, 103392. [CrossRef]
30. Alkan, S.; Sehitoglu, H. Prediction of transformation stresses in NiTi shape memory alloy. *Acta Mater.* **2019**, *175*, 182–195. [CrossRef]
31. Sidharth, R.; Celebi, T.B.; Sehitoglu, H. Origins of functional fatigue and reversible transformation of precipitates in NiTi shape memory alloy. *Acta Mater.* **2024**, *274*, 119990. [CrossRef]
32. Kong, L.J.; Wang, B.; Meng, X.L.; Gao, Z.Y. Texture evolution, microstructure, and superelastic properties of different cold-rolled Ti-Zr-Nb-Sn strain glass alloys. *Mater. Charact.* **2022**, *193*, 112309. [CrossRef]
33. Levitas, V.I. Phase-field theory for martensitic phase transformations at large strains. *Int. J. Plast.* **2013**, *49*, 85–118. [CrossRef]
34. Drakopoulos, M.; Connolley, T.; Reinhard, C.; Atwood, R.; Magdysyuk, O.; Vo, N.; Hart, M.; Connor, L.; Humphreys, B.; Howell, G.; et al. I12: The Joint Engineering, Environment and Processing (JEEP) beamline at Diamond Light Source. *J. Synchrotron. Radiat.* **2015**, *22*, 828–838. [CrossRef] [PubMed]
35. Jung, D.S.; Donath, T.; Magdysyuk, O.; Bednarcik, J. High-energy X-ray applications: Current status and new opportunities. *Powder. Diffr.* **2017**, *32*, 22–27. [CrossRef]
36. Hart, M.L.; Drakopoulos, M.; Reinhard, C.; Connolley, T. Complete elliptical ring geometry provides energy and instrument calibration for synchrotron-based two-dimensional X-ray diffraction. *J. Appl. Crystallogr.* **2013**, *46*, 1249–1260. [CrossRef] [PubMed]
37. Basham, M.; Filik, J.; Wharmby, M.T.; Chang, P.C.Y.; El Kassaby, B.; Gerring, M.; Aishima, J.; Levik, K.; Pulford, B.C.A.; Sikharulidze, I.; et al. Data Analysis WorkbeNch (DAWN). *J. Synchrotron. Radiat.* **2015**, *22*, 853–858. [CrossRef]
38. Filik, J.; Ashton, A.W.; Chang, P.C.Y.; Chater, P.A.; Day, S.J.; Drakopoulos, M.; Gerring, M.W.; Hart, M.L.; Magdysyuk, O.V.; Michalik, S.; et al. Processing two-dimensional X-ray diffraction and small-angle scattering data in DAWN 2. *J. Appl. Crystallogr.* **2017**, *50*, 959–966. [CrossRef]
39. Church, N.L.; James, I.C.; Martin, N.; Jones, N.G. The effect of heat treatment temperature on the mechanical properties of TIMETAL® 575. *Mat. Sci. Eng. A* **2024**, *890*, 145991. [CrossRef]
40. Sun, F.; Hao, Y.L.; Nowak, S.; Gloriant, T.; Laheurte, P.; Prima, F. A thermo-mechanical treatment to improve the superelastic performances of biomedical Ti-26Nb and Ti-20Nb-6Zr (at.%) alloys. *J. Mech. Behav. Biomed.* **2011**, *4*, 1864–1872. [CrossRef]
41. Church, N.L.; Talbot, C.E.P.; Connor, L.; Michalik, S.; Jones, N.G. In Situ Studies of α Evolution During Cyclic Testing of Ti-24Nb-4Zr-8Sn. In Proceedings of the 15th World Conference on Titanium (Ti-2023), Edinburgh, UK, 12–16 June 2023.
42. Church, N.L.; Jones, N.G. The influence of stress on subsequent superelastic behaviour in Ti2448 (Ti-24Nb-4Zr-8Sn, wt%). *Mat. Sci. Eng. A* **2022**, *833*, 142530. [CrossRef]
43. Gao, J.J.; Thibon, I.; Castany, P.; Gloriant, T. Effect of grain size on the recovery strain in a new Ti-20Zr-12Nb-2Sn superelastic alloy. *Mat. Sci. Eng. A* **2020**, *793*, 139878. [CrossRef]
44. Kim, H.Y.; Sasaki, T.; Okutsu, K.; Kim, J.I.; Inamura, T.; Hosoda, H.; Miyazaki, S. Texture and shape memory behavior of Ti-22Nb-6Ta alloy. *Acta Mater.* **2006**, *54*, 423–433. [CrossRef]

45. Lee, W.S.; Chen, T.H.; Lin, C.F.; Luo, W.Z. Dynamic Mechanical Response of Biomedical 316L Stainless Steel as Function of Strain Rate and Temperature. *Bioinorg. Chem. Appl.* **2011**, *2011*, 173782. [CrossRef]
46. Inamura, T.; Shimizu, R.; Kim, H.; Miyazaki, S.; Hosoda, H. Optimum rolling ratio for obtaining {001} < 110 > recrystallization texture in Ti–Nb–Al biomedical shape memory alloy. *Mater. Sci. Eng. C* **2016**, *61*, 499–505.
47. Xiao, J.F.; Shang, X.K.; Hou, J.H.; Li, Y.Y.; He, B.B. Role of stress-induced martensite on damage behavior in a metastable β titanium alloy. *Int. J. Plast.* **2021**, *142*, 103103. [CrossRef]
48. Dong, R.; Tan, Y.; Hou, H.; Ren, G.; Wang, N.; Zhao, Y. Stress-Induced α'' Martensite and Its Variant Selection in a Metastable β Titanium Alloy under an Uniaxial Compression. *J. Mater. Res. Technol.* **2024**, *30*, 1795–1799. [CrossRef]
49. Sander, B.; Raabe, D. Texture inhomogeneity in a Ti–Nb-based β-titanium alloy after warm rolling and recrystallization. *Mater. Sci. Eng. A* **2008**, *479*, 236–247. [CrossRef]
50. Reed, O.G.; Church, N.L.; Talbot, C.E.P.; Connor, L.; Michalik, S.; Jones, N.G. The degredation mechanism of Ti-Nb-Zr-Sn alloys during cyclic testing. In Proceedings of the 15th World Conference on Titanium (Ti-2023), Edinburgh, UK, 12–16 June 2023.
51. Lieberman, D.S.; Wechsler, M.S.; Read, T.A. Cubic to Orthorhombic Diffusionless Phase Change-Experimental and Theoretical Studies of Aucd. *J. Appl. Phys.* **1955**, *26*, 473–484. [CrossRef]
52. Cao, M.Z.; He, B.B. A Review on Deformation Mechanisms of Metastable β Titanium Alloys. *J. Mater. Sci.* **2024**, *59*, 14981–15016. [CrossRef]

Disclaimer/Publisher's Note: The statements, opinions and data contained in all publications are solely those of the individual author(s) and contributor(s) and not of MDPI and/or the editor(s). MDPI and/or the editor(s) disclaim responsibility for any injury to people or property resulting from any ideas, methods, instructions or products referred to in the content.